Journal of Alloys and Compounds 1032 (2025) 181173

Contents lists available at ScienceDirect

Journal of Alloys and Compounds

journal homepage: www.elsevier.com/locate/jalcom

Coherent and semi-coherent interfaces induced high strength-plasticity compatibility of $(Ti+Al)_p$/AZ31 composites prepared by laser melt injection

Zhenzhen Gui [a,b,*], Chaowen Guo [a], Liu Cao [a], Fan Zhang [a], Dexin Chen [c], Tao Zhang [d,**], Teng Shen [a,b], Jianhui Zhang [a,b], Tao Zou [a,b,*], Dejian Liu [e,**]

[a] School of Mechanical and Electrical Engineering, Guangzhou University, Guangzhou Higher Education Mega Center, 230 Wai Huan Xi Road, Guangzhou 510006, China
[b] Yangjiang Polytechnic, 213 Dongshan Road Jiangcheng District, Yangjiang 529566, China
[c] Institute of Advanced Wear & Corrosion Resistant and Functional Materials, Jinan University, 601 Huangpu Avenue West, Guangzhou 510632, China
[d] School of Phycical and Materials Science, Guangzhou University, Guangzhou Higher Education Mega Center, 230 Wai Huan Xi Road, Guangzhou 510006, China
[e] State Key Laboratory of Materials Processing and Die & Mould Technology, Huazhong University of Science and Technology, Wuhan 430074, China

ARTICLE INFO

Keywords:
Laser melt injection
Magnesium matrix composites
Mixed particles reinforcement
Interfacial bonding

ABSTRACT

Magnesium matrix composites (MMCs) have the advantages of lightweight properties, excellent mechanical properties, and biocompatibility. To achieve deformation coordination and high strength-plasticity compatibility of MMCs, pure Ti is a good candidate for reinforcement. However, Ti and Mg can neither form solid solution nor undergo chemical reactions. This work proposes a new method based on laser melt injection for preparing $(Ti+Al)_p$/AZ31 composites using commercial hot-rolled AZ31 as the matrix. Pre-mixed Ti and Al particles, which can be quantitatively adjusted, are injected into the laser melting hot-rolled AZ31 matrix. Ti particles are uniformly distributed in the matrix, and a metallurgical bonding with interfacial precipitates between unmelted Ti particles and the matrix is established through the molten Al particles. At the interfaces, Ti/Al_3Ti form a coherent orientation relationship, while $TiMnSi_2/Mg_2Si$ and $TiMnSi_2/Ti$ are semi-coherent. The results showed that the YS, UTS and EL of $(Ti+6\ wt\%Al)_p$/AZ31 composites were 186.6 MPa, 243.6 MPa and 17.2 %, respectively, which were enhanced by 48.2 % and 21.8 % for YS and UTS, compared to AZ31 matrix. Meanwhile, the $(Ti+Al)_p$/AZ31 composites present better wear resistance than that of the hot-rolled AZ31 matrix. The very fine grains of the rapid laser forming process contribute to the excellent comprehensive performance, and the nanoscale precipitates with coherent or semi-coherent interfaces produce strengthening effect.

1. Introduction

With the advantages of lightweight properties, excellent mechanical properties, and biocompatibility, magnesium matrix composites (MMCs) are the most attractive substitute materials in automobile, aerospace, biomedical, and other fields [1–5]. To improve strength and wear resistance, ceramic particles such as SiC [6,7], TiC [8,9], B_4C [10] and Al_2O_3[11] are widely used in MMCs. However, ceramic particles have poor deformation characteristics as well as great difference in thermal expansion with metal matrix. Besides, interface connection of ceramic particles to the metal matrix often tends to be incoherent [12,13]. Thus, the application of ceramic particles has a tendency to deteriorate the plasticity of MMCs. While metal particles have good ductility and the coefficient of thermal expansion (CTE) is relatively less different than magnesium (Mg) alloy matrix. Metal particles can achieve good deformation coordination by forming a strong metallurgical interfacial bond with the substrate, so as to avoid the plasticity deterioration of the ceramic particles reinforcement.

With the properties of high strength and ductility, metal particles such as Ti [14–17], Ni [18], Cu [19] and Fe [20] can be used to strengthen magnesium matrix. With the same hexagonal closepacked structure as Mg, Ti particles are easy to achieve deformation coordination, thus being regarded a good candidate for MMCs [21,22]. Yu et al. [23] found coherent interfaces between the (101)Ti and (100)Mg, and

* Corresponding authors at: School of Mechanical and Electrical Engineering, Guangzhou University, Guangzhou Higher Education Mega Center, 230 Wai Huan Xi Road, Guangzhou 510006, China
** Corresponding authors.
E-mail addresses: zhenzhengui@gzhu.edu.cn (Z. Gui), zhangtao@gzhu.edu.cn (T. Zhang), tzou@gzhu.edu.cn (T. Zou), djliu@hust.edu.cn (D. Liu).

https://doi.org/10.1016/j.jallcom.2025.181173
Received 16 April 2025; Received in revised form 13 May 2025; Accepted 22 May 2025
Available online 23 May 2025
0925-8388/© 2025 Elsevier B.V. All rights are reserved, including those for text and data mining, AI training, and similar technologies.

semi-coherent interfaces between (002)Ti and (002)Mg through high-resolution transmission electron microscope (HRTEM). However, since Ti and Mg can neither form solid solution nor undergo chemical reactions, the direct Ti/Mg interfacial bonding is often weak, and further plastic processing is needed to improve the comprehensive performance of MMCs. Ye et al. [24] prepared MMCs with added micron-sized Ti particles by powder metallurgy, and the nanoscale MgO layer formed between the Ti particles and the Mg matrix helped to improve the interfacial bond strength. Pu et al. [21] prepared Ti/AZ91 composites and identified that the Al element formed the Al3Ti interface layer which helps to transfer stresses more efficiently and promotes coordinated dislocation motion. Ti particles reinforced MMCs were prepared by Ye et al. [25] using hot pressing, resulting in enhanced overall mechanical properties compared to the AZ31 matrix, attributed to grain refinement and strong bonding interface. Grain refinement is effective in both enhance the strength and ductility of the Mg alloys, in which the increased area of grain boundaries can impede dislocations movement and the grain boundaries tend to coordinate mutually during plastic deformation [26]. The improvement of the mechanical properties of MMCs in several of the above methods was contributed by plasticity process. Gui et al.[15] studied the Ti/Mg-RE and showed greater wear resistance compared to Mg-RE matrix and tensile strength reaching 160 MPa. The main reason for the failure to strengthen the mechanical properties could be the less strong interfacial bonding between Mg-RE and Ti particles. To enhance the strength and wear resistance of Ti particles simultaneously, it is essential to further enhance the interfacial bonding between the Ti particles and the matrix. In the Ti particles reinforced AZ series matrix, Al is easily enriched at the interface of Ti particles [24,25]. Based on the Al-Ti [27] binary phase diagram, Al-Ti is able to form different kinds of intermetallic compounds, thus a good metallurgical interfacial bonding can be formed between Ti and Al [28,29]. In Ti particles reinforced Mg-3Al-1Zn composites, TiAl nanolayers are formed at the Ti/Mg interface and the misfit between TiAl and Mg matrix is low. In addition, many Al_2Ti nanoparticles are formed at TiAl/Mg interface, and Al_2Ti nanoparticles have a semi-coherent lattice relationship with TiAl layer and Mg matrix, respectively [24]. These Al-containing precipitated phases resulted in strong interfacial bonding between the Ti particles and the Mg matrix. Besides, the eutectic reaction occurred between Al and Mg at 437°C [30]. Therefore, Al can not only react with Ti and Mg, but also act as a transition element between the Mg/Ti interface and promote the formation of a well-formed metallurgical interface between Mg and Ti.

Comparison with Al element, the Zn element also has the property of reacting with both Mg and Ti. Zhang et al. [31] researched the compressive strength and plasticity of Zn-3Mg-1Ti alloys and found that the plasticity of Zn-3Mg-1Ti alloys reached only about 8 %, probably caused by the presence of the Mg_2Zn_{11} phase. In addition, Cu element can also be acted as a binding agent at the Mg-Ti interface to enhance the interfacial bonding between Mg and Ti because of its significant solid solubility with Ti and Mg. However, the preparation of Mg/Ti/Cu composites by powder metallurgy method by Kumar et al. [32] showed that the addition of Cu decreases the strength, hardness and wear rate of magnesium matrix composites, although it can increase the thermal conductivity. Therefore, the Al element is more suitable as a transition element between Mg-Ti than the Zn and Cu element.

In this paper, the pre-mixed $(Ti+Al)_p$ particles with different mass fractions of Al were used as reinforcement particles to be injected into the laser molten pool of the hot-rolled AZ31. The Al particles were melted in the micro molten pool, served as the interfacial transition between Ti particles and the matrix, and promoted the formation of a strong metallurgical interfacial bonding. The influence of laser process parameters on the microstructure of single pass melt injection layers prepared with different mass ratios of Ti and Al mixed particles was systematically researched, and $(Ti+Al)_p$/AZ31 composites with uniform particle distribution were successfully prepared by exploring the preferred process window. The effect of Al particles melted under high temperature micro melt pool as a transition element on the interfacial reaction between Ti particles and Mg matrix was discussed, and the mechanical properties of $(Ti+Al)_p$/AZ31 composites with different mass ratios were studied. It was shown that compared to the Mg matrix, the $(Ti+Al)_p$/AZ31 MMCs prepared by laser melt injection formed a stronger metallurgical interfacial bonding under rapid solidification condition, and achieved strength and plasticity enhancement synergistically.

2. Materials and methods

2.1. Preparation of composite materials

The matrix for the laser melting experiments was a commercial hot-rolled AZ31 magnesium alloy with the chemical composition shown in Table 1. The pre-mixed particles of spherical Ti (15–53μm) and Al (15–53μm) were used as raw materials as shown in Fig. 1. Ti and Al mixed particles of different mass fractions were prepared: Ti+ 6 wt%Al, Ti+ 13 wt%Al, Ti+ 20 wt%Al, where (Ti+6 wt%Al) indicates that the mass fraction of Al particles in (Ti+Al) mixed particles is 6 %, and so on. The prepared three groups of composites were $(Ti+6\ wt\%Al)_p$/AZ31, $(Ti+13\ wt\%Al)_p$/AZ31, and $(Ti+20\ wt\%Al)_p$/AZ31, which were named as T6AC, T13AC, and T20AC, respectively. The EDS images of three different proportions of Ti and Al mixed particles after mixing have been added to Fig. 1(e, f, g), where red represents Ti particles and green represents Al particles. The Ti and Al mixed particles in this study are relatively uniformly dispersed, which helps to maintain good mixing and flowability of the particles during the laser melting and powder feeding process.

The schematic diagram of the experimental platform for this experiment is shown in Fig. 2. Fibre lasers propagate a Gaussian beam, and KUKA CR-60HA six-axis robot performed the laser scanning. The pre-mixed particles of Ti and Al were taken out with inert gas (Ar) and injected into the molten pool of the hot-rolled AZ31 through the coaxial powder feeding head. In order to reduce the high reflections, the laser generator was tilted at 5° for the experiments. The experimental procedure in detail is described by our earlier work [15].

2.2. Characterisation and testing

The cross sections of the $(Ti+Al)_p$/AZ31 samples were cut, ground, and polished. The microstructure of the samples was analyzed by optical microscope (OM, Zeiss Axio Vert.A1) and scanning electron microscope (SEM, ZEISS G460, equipped with BRUKER spectrometer). X-ray diffractometer (XRD, Empyrean) was used for phase analysis, and the diffraction angle range was 30°-80°. Using Cu target (Kα) as the radiation source, the working voltage is 40 kV, and the scanning step size is 5 °/min. The XRD data measured by the instrument was analyzed using Jade 6 software and compared with standard PDF cards to determine the phase. The interfacial microstructure of the $(Ti+Al)_p$/AZ31 composites was further analyzed by transmission electron microscope (TEM, Thermofisher Talos F200X, equipped with SuperX G2 energy dispersive spectroscopy (EDS)).

The friction and wear test was carried out under the UMT-Tribolab friction and wear testing machine with the load of 15 N and the sliding speed of 10 mm/s. The operation was performed under the Si_3N_4 friction pair for 10 minutes by ball-on-flat mode. TThe abrasion marks were observed by Super-Depth-of-Field Microscope (KEYENCE VHX-5000). The SHIMADZU AGX V universal testing machine equipped with a video extensometer was used for tensile test, and the tensile rate was set at 0.3 mm/min. Tensile testing samples are taken from the

Table 1
Composition of the commercial hot-rolled AZ31 alloy.

Element	Al	Zn	Mn	Si	Cu	Fe	Ni	Mg
Percent	2.93	0.82	0.61	0.08	0.01	0.003	0.001	Bal

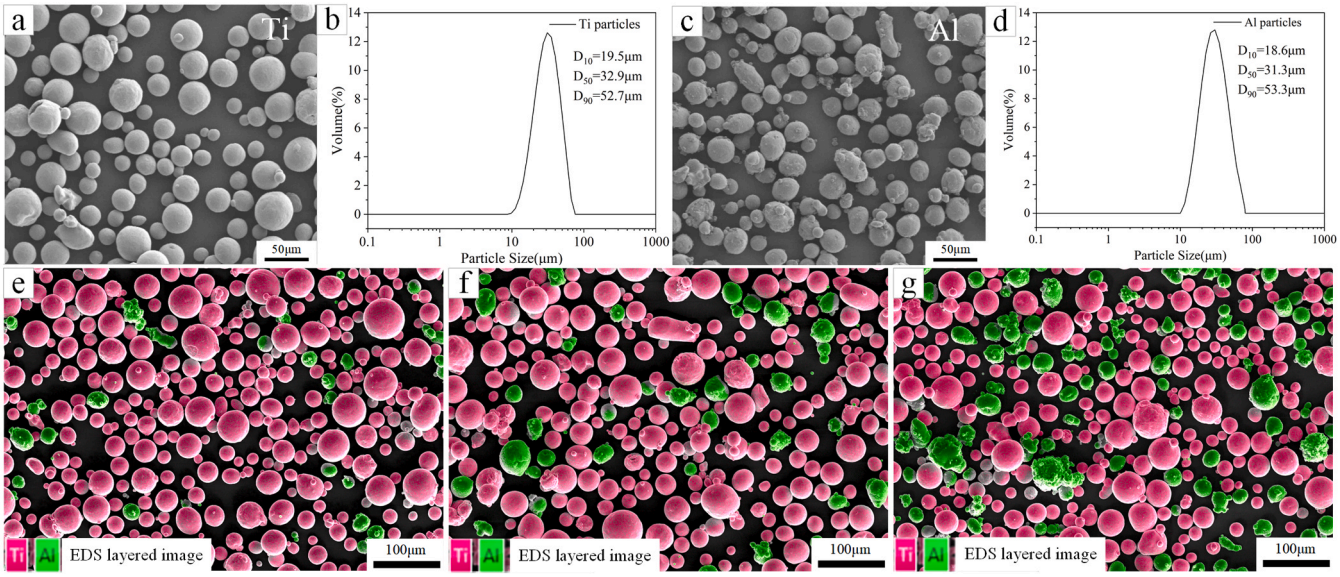


Fig. 1. (a, c) SEM image of Ti and Al particles, (b, d) size distributions of Ti and Al particles, (e-g) EDS images of T6AC, T13AC, T20AC mixed powders respectively.

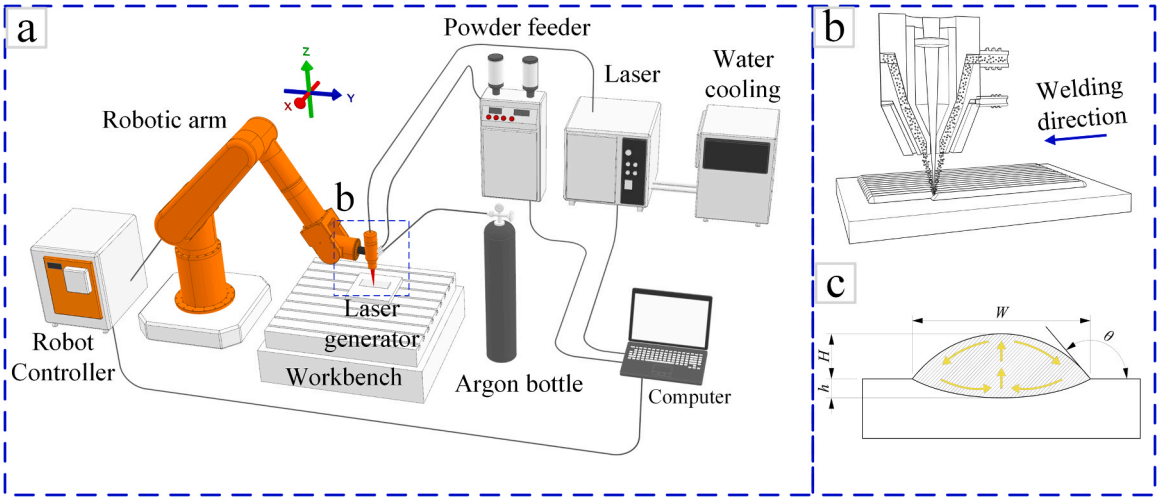


Fig. 2. (a) Laser melt injection system, (b) schematic diagram of laser melt injection process, (c) schematic diagram of internal flow of molten pool.

composites layer and the hot-rolled AZ31 alloy, and the widths, thicknesses, and gauge length are about 4 mm, 0.8 mm, and 5 mm, respectively. Three groups of samples with three repeats for each group were tested to calculate the average values of the YS, UTS and elongation (EL).

3. Results

3.1. Microstructure of the $(Ti+Al)_p$/AZ31 composites

The phases of Mg matrix and composites were analysed by XRD in Fig. 3(a) The result shows that the matrix phases of the hot-rolled AZ31 are α-Mg and β-$Mg_{17}Al_{12}$, while most of the Ti in the composites did not

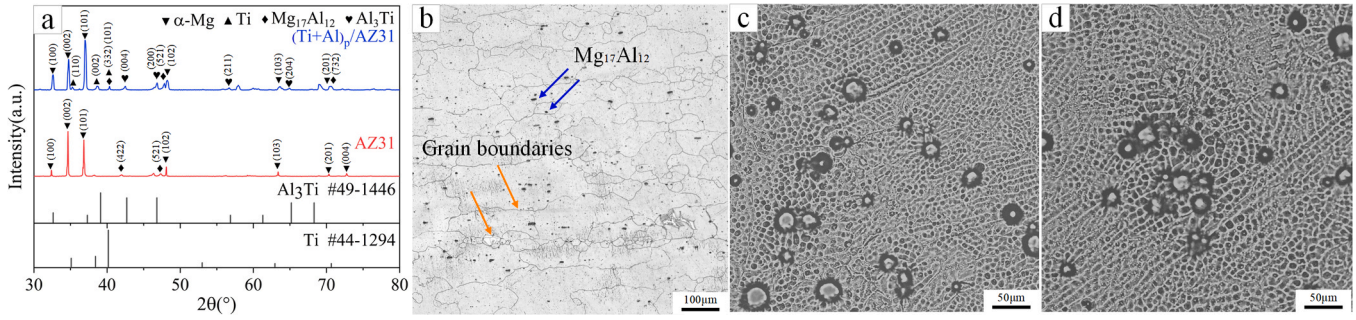


Fig. 3. (a) The XRD analysis to hot-rolled AZ31 and composites, (b, c, d) OM morphology of the AZ31 matrix, T6AC and T20AC.

melt and maintained consistency with the peak of pure Ti, and Al_3Ti is formed by the reaction of some Ti particles with molten Al particles in the laser molten pool. Fig. 3(b) shows the OM morphology of the hot-rolled AZ31. Combined with XRD analysis, the dark particles phase in hot-rolled AZ31 is identified as β-$Mg_{17}Al_{12}$. Compared with the hot-rolled AZ31, the molten pool grains showed a significant refinement as shown in Fig. 3(c). Using ImageJ image processing software, multiple line segments were intercepted along the transverse and longitudinal directions of the grains presented in Fig. 3(b, c, d), and the magnesium grain size was statistically calculated by the truncation method, which refined the magnesium grain size from 56.8 μm to 3.3 μm and 6.5 μm.

To study the effect of Al content on the molten pool morphology under laser melting conditions., the cross-sectional OM morphology of the $(Ti+Al)_p$/AZ31 composites is shown in Fig. 4. It has been confirmed by SEM/EDS that the particles in the welds are all unmelted Ti particles, indicating that the intermediate Al element of Ti and Mg, with variable content, participate in micro melt pool metallurgy. A highly dynamic Marangoni flow melt pool with extremely high temperature gradients was formed, resulting in the formability of the micro-molten pool changing dynamically along the process [33,34]. When the Al content in the mixed particles is low, the excess weld metal is low (Fig. 4.a1–a4), the primary reason is that most of the Ti particles remained unmelted, with only a small portion of Al particles melting and absorbing heat, leading to a relatively high temperature in the molten pool system [35]. The low excess weld metal is also observed at 20 % Al content (Fig. 4. c1–c4), which is mainly due to the reduction in Ti particles into the molten pool, and a large quantity of Al particles are melted in the high temperature molten pool. The molten pool surface tension reduces with increasing Al content [36]. Therefore, when the content of Al is moderate (Fig. 4.b1–b4), the prepared T13AC has a relatively uniform Ti particle distribution and a good weld morphology. In addition, the area ratios of Ti particles in the welds of the T6AC - T20AC fluctuated in the range of 10 % - 40 % by calculation of binarization, as shown in Fig. 4 (a1–c4). Further, the most uniform Ti particle distribution in the molten pool was shown under 1800 W. Considering also that there is energy accumulation in the laser melting process, T6AC multi-pass welds were

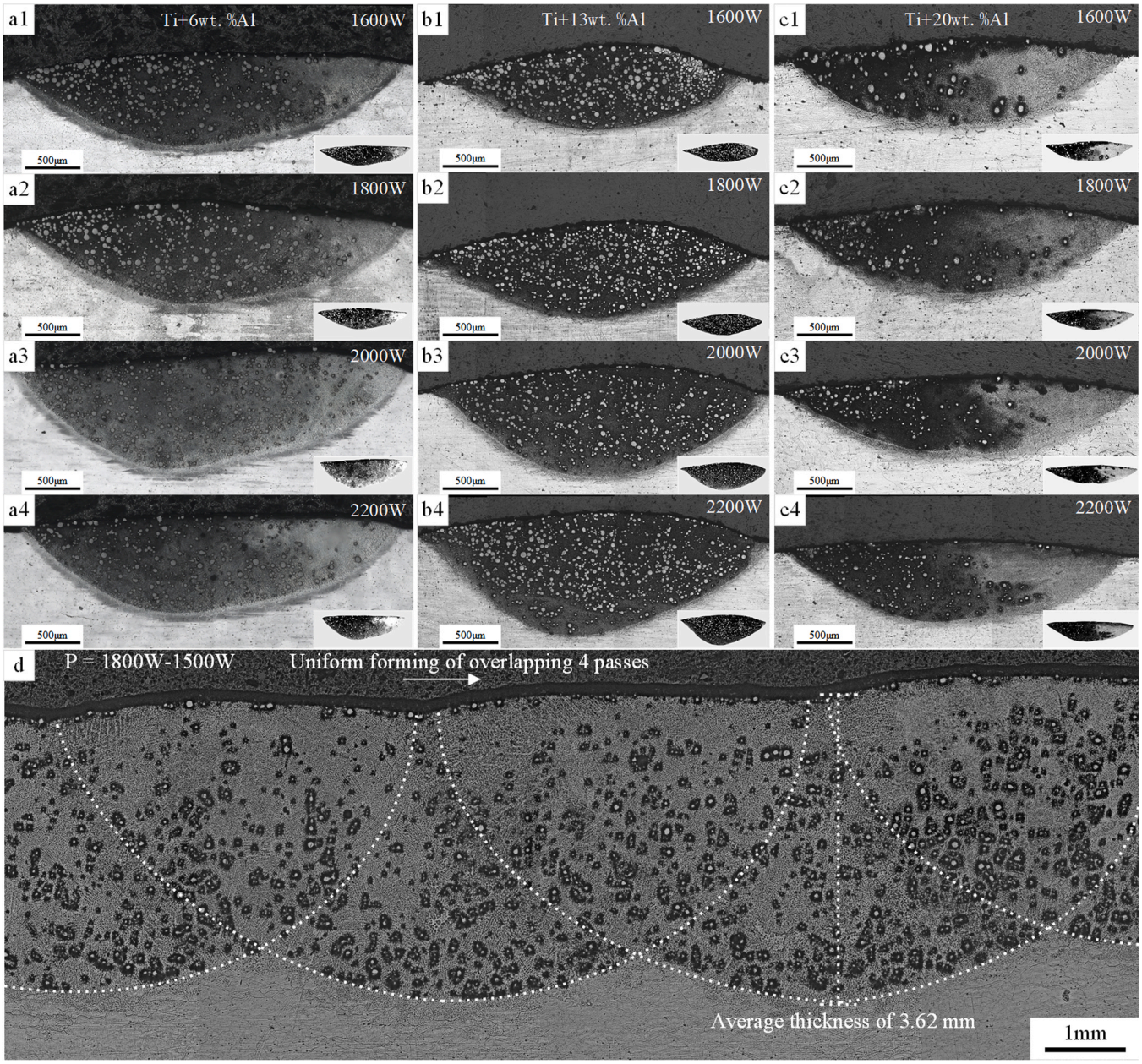


Fig. 4. Microstructure of the $(Ti+Al)_p$/AZ31 composites: (a1–a4) T6AC, (b1–b4) T13AC, (c1–c4) T20AC, (d) T6AC composites multi-pass welds.

prepared with variable power from 1800 W to 1500 W, as shown in Fig. 4(d). The average thickness of the T6AC multipass melt injection layer was measured to be 3.62 mm. The single-pass welds were prepared and partially resolidified based on an appropriate laser offset in the next thermal cycling; thus, large-area multi-pass welds were formed without obvious cracks, pores and other defects.

Effects of parameters on melting width, melting depth and excess weld metal of the single-pass welds of the $(Ti+Al)_p$/AZ31 composites are shown in Fig. 5. As shown in Fig. 5, the $(Ti+Al)_p$/AZ31 composites of 6 wt% and 20 wt% Al exhibit a similar behavior, which is that the molten pool size shows a fluctuating change with the increase of laser power. In contrast, the molten pool size of $(Ti+Al)_p$/AZ31 composites with 13 wt% Al shows an increasing trend with increasing laser power. This different pattern of change is mainly attributed to the modulation of the thermodynamic behaviour of the molten pool by the difference in Ti and Al content. At low Al content (6 wt%), the high percentage of unmelted Ti particles affects the internal thermal conductivity of the melt pool; at high Al content (20 wt%), the rapid melting of excess Al particles reduces the surface tension of the melt pool, and the above factors lead to the breakage of the thermodynamic equilibrium of the melt pool with the further increase of power (after 1800 W), with the oscillating characteristics of the melt width and melt depth. In contrast, the moderate melting of Al particles in $(Ti+Al)_p$/AZ31 composites with 13 wt% Al reduces the melt surface tension and promotes the stability of Marangoni convection, and at the same time, the distribution density of unmelted Ti particles maintains the effective heat conduction in the molten pool, and therefore, the melt depth and melt width show a linear growth trend. The above variation rule of the melt pool is also one of the reasons that prompted this study to adopt 1800 W laser power for multipass lap welding.

The SEM of T13AC is shown in Fig. 6(a–c). The upper and middle parts of the composites are the main channels for heat dissipation, and the value of temperature gradient/solidification rate ratio is small [37], resulting in a structure mainly consists of equiaxed grains. The molten pool bottom is largely influenced by rapid solidification and has a large gradient/solidification rate ratio, leading to the formation of columnar crystals vertical across the fusion line. The Ti particles did not melt and maintained the original spherical shape, while most Al particles reacts with Mg to produce a large quantity of $Mg_{17}Al_{12}$ and some Al elements were enriched around the interface of the Ti particles, in Fig. 6(d-i). According to the Al-Ti diffusion mechanism, the diffusion coefficient of liquid Al in solid Ti ($D_{Al/Ti}$=2.5 $\times10^{-13}$ $m^2 \bullet S^{-1}$) is considerably larger compared to the diffusion coefficient of the Ti element in the Al element ($D_{Ti/Al}$=4.7 $\times10^{-17}$ $m^2 \bullet S^{-1}$) [38], which means that Al atoms can diffuse through the reaction layer to Ti layer. Thus, the reaction between Ti and Al continues. To study Al elemental diffusion with change in laser power, line-scan EDS analysis was used and shown in Fig. 7(a-h). Temperature is the most important factor affecting the diffusion rate. As the temperature increases, the diffusion rate rises, leading to a higher number of vacancies in the metal, which is conducive to the progress of diffusion [39,40]. As can be observed from Fig. 7(e–h), Al element diffusion zone at the Ti interface increases from 2.5 μm to 4.6 μm as the energy increases from 1600 W to 2200 W. The diffusion zone promotes the reaction between Al and Ti to improve the metallurgical binding strength.

3.2. Interfacial properties

The TEM bright field (BF) images of the interface around the Ti particles of $(Ti+6\ wt\%Al)_p$/AZ31 composite are demonstrated in Fig. 8 (a,b). The distribution of elements on the interface was shown in Fig. 8 (d-h). From the region within dashed line in Fig. 8(a), an Al enriched layer with an average thickness of about 34 nm on the side of Ti particles can be observed. In Fig. 8(b), a rod-like structure with a size of about 227 nm × 47 nm is precipitated on the side of Ti particles. The rod-like structure is composed of enriched Ti, Mn, and Si. The above results indicate that the element diffusion and chemical reactions forming Al-Ti and Ti-Mn-Si compounds occurred during the laser melt injection process.

For revealing interface integration, phase identification was further performed by HRTEM, as shown in Figs. 9 and 10. In Fig. 9(a), a distinct interface zone is divided into region I and II. The d1 and d2 spacings measured in region I are 0.1362 nm and 0.1166 nm, and in region II are 0.2568 nm and 0.2250 nm, respectively. The analysis result of diffraction spots at the interface (the inset image in Fig. 9(a, d)) indicates that region I and II are Al_3Ti and Ti, respectively. Namely, Al_3Ti is produced at the Al enriched layer in Fig. 8(a). Fig. 9(a) shows that the interfacial orientation relationship between Ti and Al_3Ti is$(\bar{1}10)Ti//(13\bar{2})Al_3Ti$ and$[111]Ti//[514]Al_3Ti$, and a coherent interface is formed between the two phases of Al_3Ti and Ti. In addition, the lattice fringe images corresponding to Al_3Ti are obtained by Inverse Fast Fourier Transform (IFFT), and the edge dislocation formed by lattice mismatch can be found, as shown in Fig. 9(c, f). Meanwhile, Fig. 9(b) corresponds to the HRTEM image (region III and IV) of region B of Fig. 8(a). The d1 and d2 spacings measured in region III are 0.1637 nm and 0.1506 nm, and in region IV are 0.2362 nm and 0.3219 nm, respectively, corresponding to the standard values of Mg and Al_8Mn_5 phase.

Fig. 10(a,d) show the HRTEM images of regions C and D in Fig. 8(b), respectively. The diffraction pattern at the interface indicates that the regions V and VI are $TiMnSi_2$ and Mg_2Si phases, respectively. According to Zhang et al.[41], the free energy of Ti-Si is 47 kJ/mol smaller compared to that between Al-Si. Therefore, the Si in local region may have reacted with Ti in place of Al.

In Fig. 10, the diffraction pattern shows that $TiMnSi_2$ has a favorable orientation relationship with Mg_2Si and Ti, namely,$(0\bar{1}0)TiMnSi_2//(\bar{1}10)Mg_2Siand(0\bar{1}0)TiMnSi_2//(01\bar{1})Ti$. Both the interfaces of $TiMnSi_2$/Mg_2Si and $TiMnSi_2$/Ti have a semi-coherent relationship. In addition, the dislocations distribution can be clearly identified through IFFT in Figs. 9 and 10, which means these precipitates could participate in deformation coordination during plastic

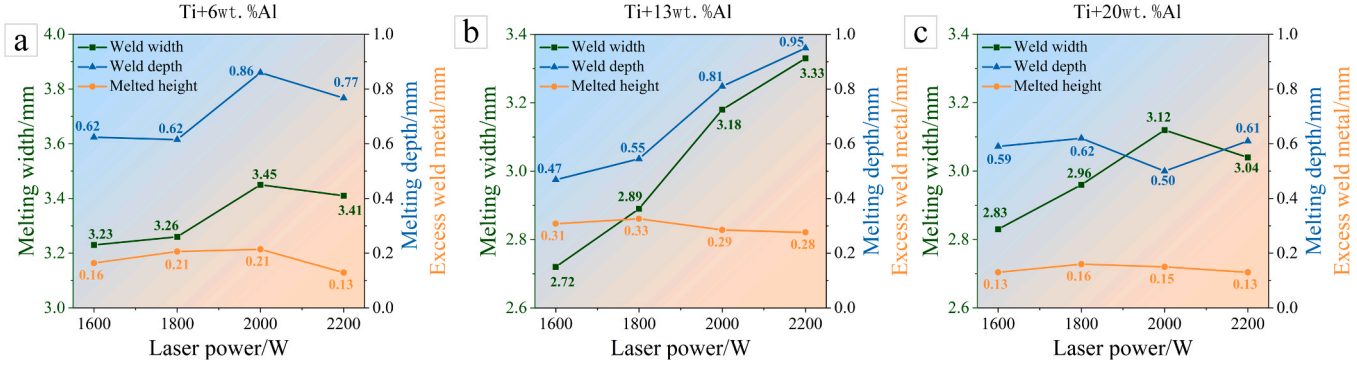


Fig. 5. Effects of parameters on melting width, melting depth and excess weld metal of the $(Ti+Al)_p$/AZ31 composites: (a) T6AC, (b) T13AC, (c) T20AC.

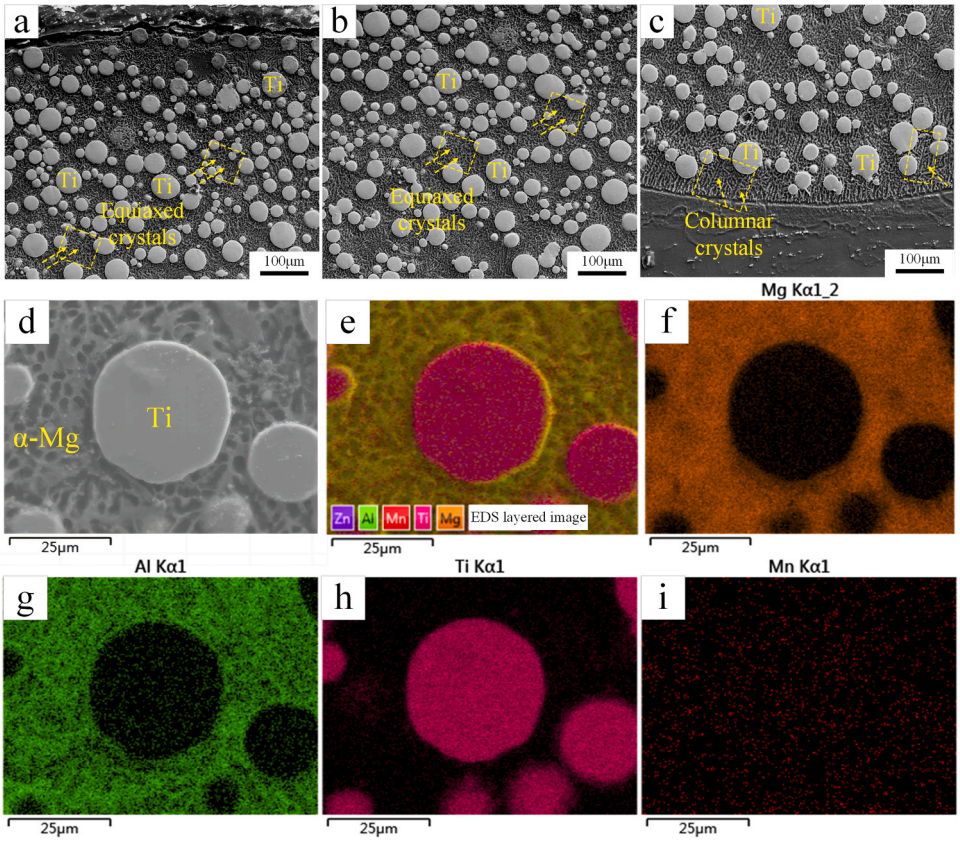


Fig. 6. (a-d) SEM of the T13AC composites. (a) upper region, (b) central region, (c) bottom region, (d) local magnification, (e-i) EDS results: (e) synthesis graph of elements distribution of Mg, Al, and Mn, (f-i) element distribution of Mg, Al, Ti and Mn respectively.

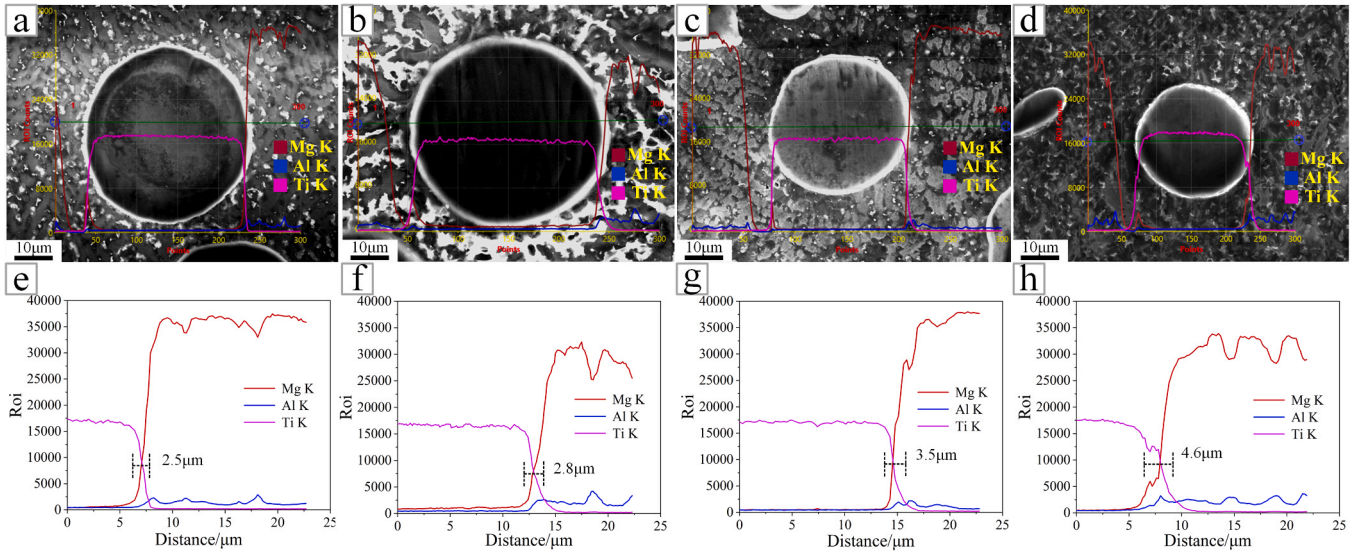


Fig. 7. EDS line scanning through the Ti particle and its interface in the T13AC composites: (a, e) 1600 W, (b, f) 1800 W, (c, g) 2000 W, (d, h) 2200 W.

deformation process to enhance the strength of the $(Ti+Al)_p$/AZ31 composites.

3.3. Mechanical properties

Fig. 11 shows typical tensile engineering stress-strain curves and tensile properties of $(Ti+Al)_p$/AZ31 composites and the hot rolled AZ31. As shown in Table 2, the T6AC with lower Al content in the mixed particles shows excellent comprehensive tensile properties, with the YS of 186.6 MPa, UTS of 243.6 MPa, and maintaining a very high EL of 17.2 %, among which the YS and UTS are 48.2 % and 21.8 % higher than those of the hot-rolled AZ31 (125.9 MPa and 200.1 MPa), respectively. Comparison of the UTS and EL of the $(Ti+Al)_p$/AZ31 composites and other MMCs with typical as-cast microstructure or laser rapid solidification microstructure is shown in Fig. 12(a) [15,42–51]. The MMCs prepared by traditional methods are hard to achieve high EL and UTS

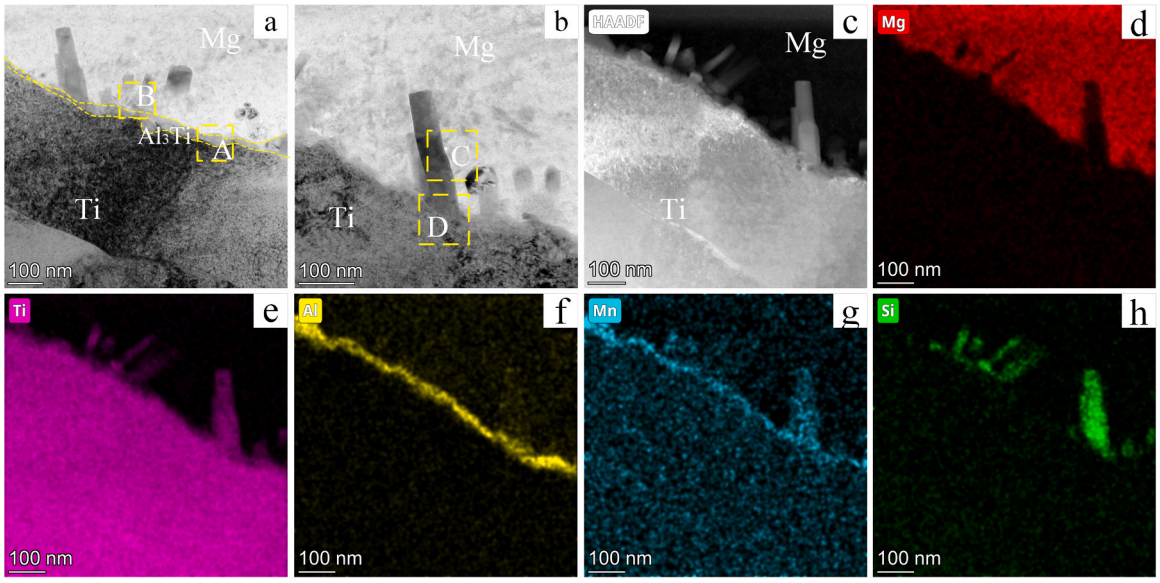


Fig. 8. (a, b) TEM BF images at the interface between Ti particles and the matrix, (c) high-angle annular dark-field (HAADF) image, EDS result of elements distribution at the interface between the Ti particle and the matrix: (d)Mg, (e)Ti, (f)Al, (g)Mn, (h)Si.

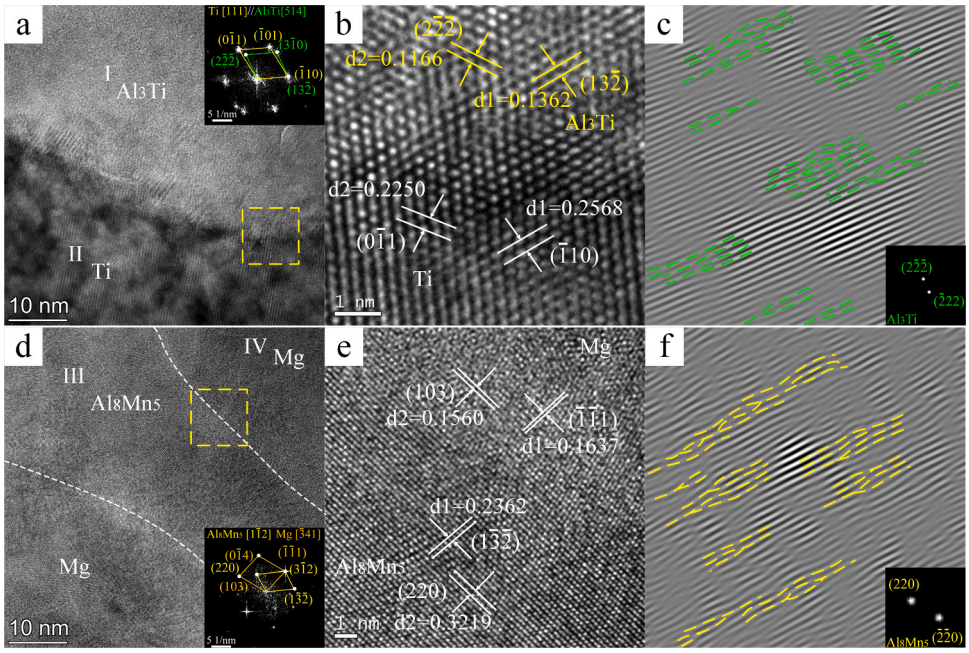


Fig. 9. (a-c and d-f): HRTEM, FFT and IFFT of regions 'A' and 'B' in Fig. 8(a).

simultaneously. For example, the ZnO/AZ31 composites [51] has a good elongation about 20 %, while its UTS is less than 200 MPa; the TC4/AZ31 composites [47] obtained a high UTS about 245 MPa, while its EL is less than 5 %.

The strain evolution of the hot-rolled AZ31 and T6AC was recorded and analyzed by video extensometer to obtain the strain cloud distribution in the loading direction. The AZ31 fractured along 90° direction from the loading direction within the gauge length at 150 s in Fig. 12(b). In contrast, the T6AC fractured along 45° direction from the loading direction within the gauge length at 260 s, which further demonstrates the plastic shear characteristics of the $(Ti+Al)_p$/AZ31 composites.

3.4. *Wear properties*

Fig. 13 displays the curve of coefficient of friction (COF) vs friction time. Fig. 13(a, b) show three repeats experiment results of the T6AC and T20AC, respectively, from which T6AC presents more stable wear process. Fig. 13(c) shows typical curves of COF vs time of the hot-rolled AZ31, T6AC, and T20AC. The average COFs of T6AC (0.2103) and T20AC (0.2228) are 22.0 % and 17.4 % lower than that of the hot-rolled AZ31 (0.2696), respectively. The wear morphology observed by the Super-Depth-of-Field Microscope is shown in Fig. 14. It can be found that the grinding cracks of the hot-rolled AZ31 and the $(Ti+Al)_p$/AZ31 composites are U-shaped with the middle lower than both sides, which is consistent with the spherical shape of the grinding ball being pressed into the samples. From the abrasion curves in Fig. 14(a4, b4, c4), the

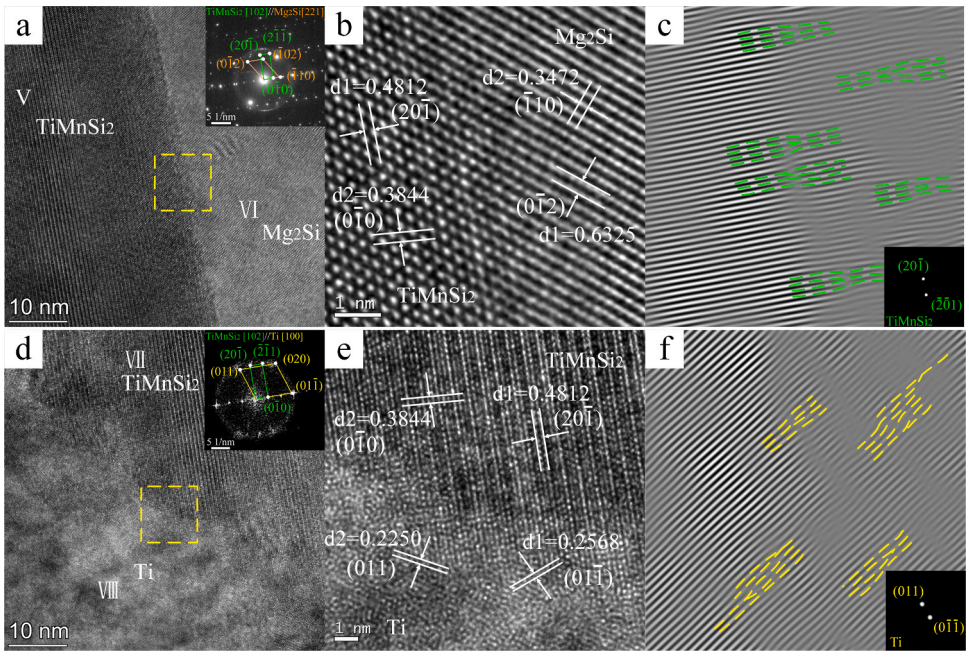


Fig. 10. (a-c and d-f): HRTEM, FFT, and IFFT of regions 'C' and 'D' in Fig. 8(b).

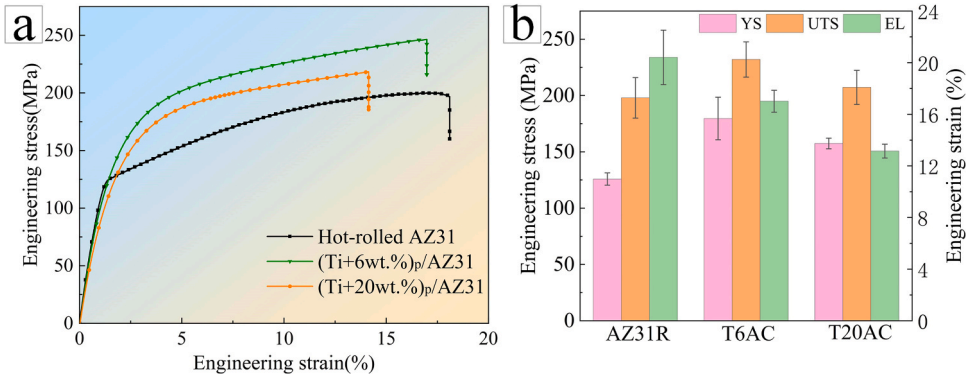


Fig. 11. (a) Typical tensile curves, (b) Mechanical property statistics of Fig. 11(a).

Table 2
Tensile properties of the composites and Mg matrix.

Samples	YS/MPa	UTS/MPa	EL/%
Hot-rolled AZ31 matrix	125.9 ± 4.7	200.1 ± 8.2	18.1 ± 1.1
(Ti+6 wt%Al)$_p$/AZ31	186.6 ± 5.4	243.6 ± 5.6	17.2 ± 0.8
(Ti+20 wt%Al)$_p$/AZ31	164.4 ± 4.4	218.2 ± 7.1	14.3 ± 0.6

abrasion depths of the hot-rolled AZ31 and (Ti+Al)$_p$/AZ31 composites were between 30 and 35 μm and 20–25 μm, respectively, which further indicates that (Ti+Al)$_p$/AZ31 composites have excellent wear resistance.

Wear morphologies of the composites and the hot-rolled AZ31 were further analyzed to confirm the reason for the wear resistance of (Ti+Al)$_p$/AZ31 composites being better than the hot-rolled AZ31. As shown in Fig. 15(a), after the load application, the grinding ball is easy to be pressed into the hot-rolled AZ31 for its relatively soft surface, resulting in a lot of parallel furrows and adhesion spalling, and serious plastic deformation of the worn surface. In addition, there are the sharp tearing angle at the edge of the grinding cracks mainly caused by the interaction of periodic positive pressure and tangential shear force of the friction progress. Fig. 15(b) shows that the grinding ball still scratches the (Ti+Al)$_p$/AZ31 composites layer, but the furrows on the worn surface become less and shallower. This is because the unmelted Ti particles distributed in the composites layer act as a harder phase, and there is a favorable bonding strength between Ti particles and the matrix, which partially hinders the friction movement. Moreover, the Ti particles hardly peeled off from the matrix to form pits. The above reasons all contribute to the resistance of friction movement, thus improving the wear resistance of (Ti+Al)$_p$/AZ31 composites.

4. Discussion

4.1. Analysis of interface between Ti particles and the magnesium matrix

According to Section 3.2, a uniform transition interface layer with a thickness of about 34 nm of Al_3Ti was formed around Ti particles. The Gibbs free energy relationship of the Al-Ti phase is $AlTi_3$->AlTi>Al_3Ti>Al_5Ti_2>Al_2Ti [52,53], while the latter two belong to the intermediate products. In addition, with a stronger chemical affinity between Ti and Al [54], the Al_3Ti with the lowest binding energy (-1.61 eV) [55] can be generated. In a crystal lattice, the diffusion activation energy is related to the binding energy that characterizes the atomic binding force [56]. The smaller the binding force, the lower the

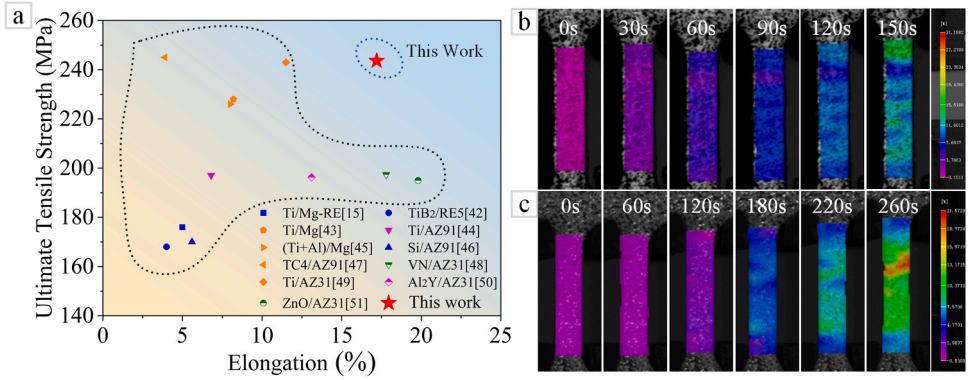


Fig. 12. (a) Comparison of mechanical properties with other MMCs [15,42–51], evolution of strain states of (b) the hot rolled AZ31 and (c)T6AC.

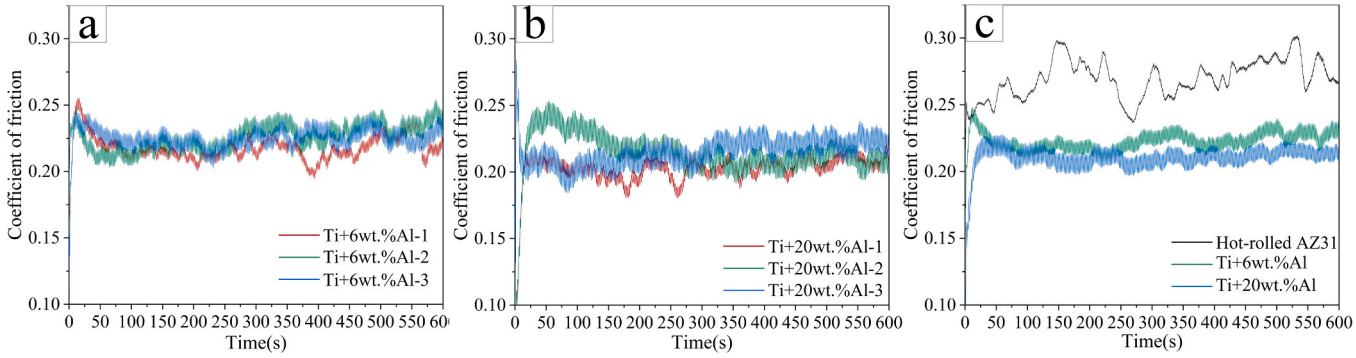


Fig. 13. COF of the hot-rolled AZ31 and series composites: (a) T6AC, (b) T20AC, (c) typical curves.

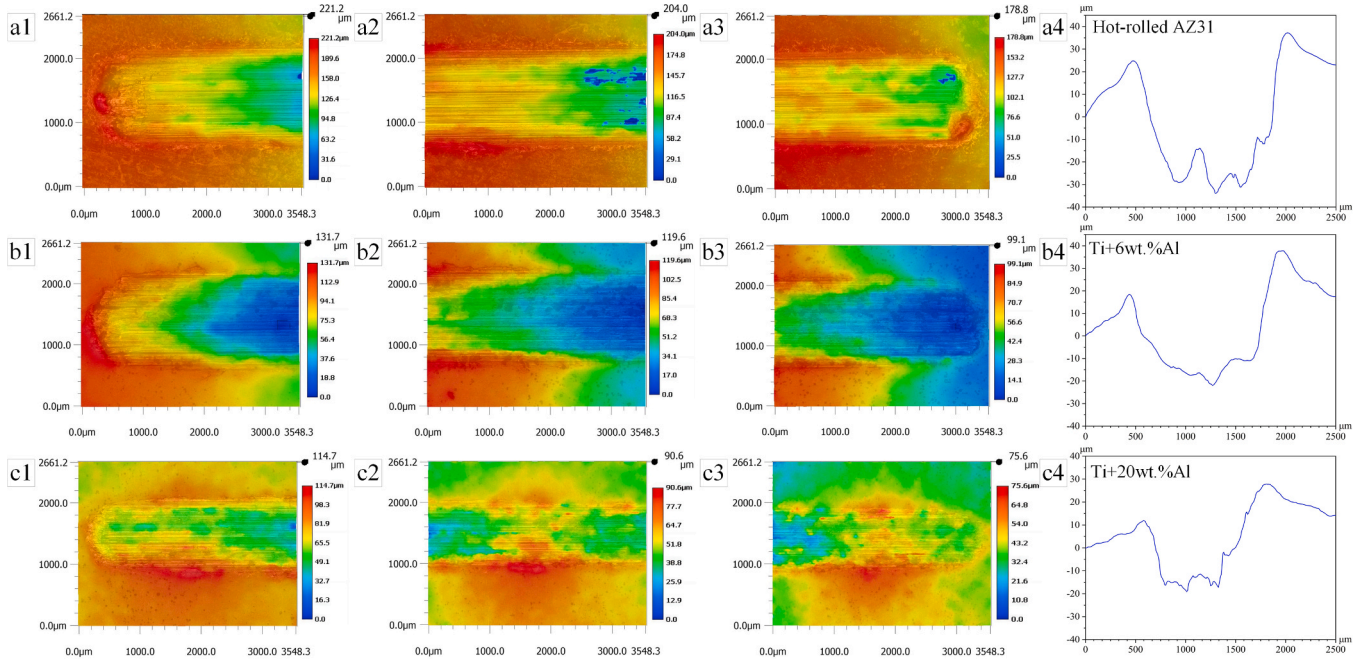


Fig. 14. Worn surface measured by Super-Depth-of-Field Microscope: (a1–a4) the hot-rolled AZ31, (b1–b4) T6AC, (c1–c4) T20AC.

diffusion activation energy and the easier the atoms can migrate. Therefore, Al_3Ti is the most easily formed among the Al-Ti phases with the reaction formula of $Ti(s) + Al(l) \rightarrow Al_3Ti(s)$. To further compare the reaction mechanism of Al_3Ti, the remaining reaction equations of Al-Ti intermetallic compounds are as follows: $Ti(s) + Al(l) \rightarrow AlTi_3(s)$, $AlTi_3(s) + Al(l) \rightarrow AlTi(s)$, $Al_3Ti(s) + Ti(s) \rightarrow Al_5Ti_2(s)$, $Ti_2Al_5(s) + Ti(s) \rightarrow Al_2Ti$ (*s*). Previous researches have demonstrated that Mg/Al_3Ti interface is semi-coherent [57,58]; thus, combined with the coherent interface of Ti/Al_3Ti, the Al_3Ti between Ti and the magnesium matrix will play a beneficial role in interfacial stress transfer during plastic deformation process. According to the Cauchy pressure and Pugh ductility index [59], the diffusion reaction layer should not be too thick, otherwise the

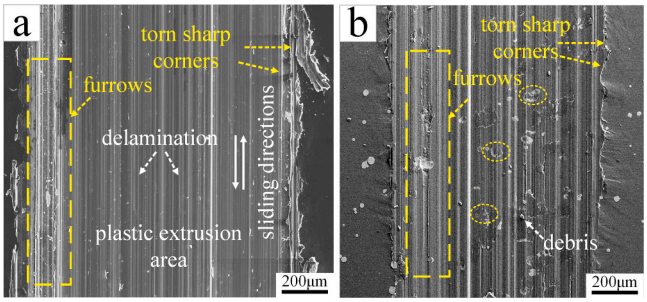


Fig. 15. SEM wear morphology of (a) hot-rolled AZ31, (b) $(Ti+Al)_p$/AZ31 composites.

interface will break prematurely due to excessive brittleness during tensile deformation. Therefore, a thickness of about 34 nm of Al_3Ti can not only serve as a transition phase to connect Ti and the magnesium matrix, but also effectively transfer interfacial stress between them.

As shown in Figs. 9 and 10, the Ti/Al_3Ti interface is coherent while the $TiMnSi_2$/Mg_2Si interface is semi-coherent. Studies pointed out that a lattice mismatch with a smaller absolute value would produce a higher strengthening effect of coherent strain [60,61]. The lattice mismatches of Al_3Ti and Ti phases can be calculated by $\varepsilon = \left|1 - \alpha_{Al_3Ti}/\alpha_{Ti}\right| \times 100\%$[62], and the result of ε is 8.3 %, where α is the lattice parameters of the phases. Meanwhile, the ε between $TiMnSi_2$ and Mg_2Si is calculated as 4.6 % by $\varepsilon = \left|1 - \alpha_{TiMnSi2}/\alpha_{Mg2Si}\right| \times 100\%$. Therefore, Al_3Ti has small lattice mismatches with Ti particles, and lattice mismatches also exist between $TiMnSi_2$ rod-like phases precipitated from Ti particle side and Mg_2Si precipitated from AZ31 side.

The above precipitated phases become a bridge connecting coherent and semi-coherent interfaces with Ti and the matrix, forming a strong metallurgical interfacial bonding, and would have a pinning effect with dislocations, thus strengthening the matrix to achieve excellent comprehensive performance.

4.2. Strengthening mechanisms of the $(Ti+Al)_p$/AZ31 composites

The refined AZ31 grains, Ti particles as well as their coherent and/or semi-coherent interfaces contribute to coordination in severe plastic deformation. Consequently, a large number of small ductile dimples emerged in the fracture, and Ti particles were completely or partially wrapped by the AZ31 matrix and no microcracks were detected, as shown in Fig. 16, which coincides with the plastic shear characteristics of fracturing at 45° of the $(Ti+Al)_p$/AZ31 composites in Fig. 12(c). As shown in Fig. 16(b-c), the large number of dimples of the AZ31 matrix and the complete or partial wrapping of Ti particles in the AZ31 matrix indicate that the interfacial bonding between the Ti particles and the AZ31 matrix is stronger than that of the AZ31 matrix. The strong metallurgical interfacial bonding formed in the laser melt pool contributes to the increase of tensile strength, and the fracture characteristics of the $(Ti+Al)_p$/AZ31 composites indicate that the damage of the composites is mainly in plastic fracture mode.

The main strengthening mechanisms of MMCs include fine grain strengthening $\Delta\sigma_{H-P}$, load transfer strengthening $\Delta\sigma_{Load}$, and thermal mismatch strengthening $\Delta\sigma_{CTE}$, which are calculated with reference values, as shown in Table 3. Under the condition of laser rapid solidification, the addition of large amount of Ti particles makes the AZ31 matrix achieve significant grain refinement, thus improving the YS of the composites. According to the Hall-Petch formula (1) [63], the value of fine grain strengthening $\Delta\sigma_{H-P}$ can be calculated as 48.9 MPa and 28.3 MPa for T6AC and T20AC:

$$\Delta\sigma_{H-P} = K(d_{AZ31}^{-1/2} - d_{Ti}^{-1/2}) \quad (1)$$

When the load was applied on the composites, the shear stress was transferred from the AZ31 matrix to the surrounding Ti particles, and the increase of YS by load transfer can be calculated by formula (2) [24], and the results are 9.4 MPa and 6.3 MPa for T6AC and T20AC composites, respectively:

$$\Delta\sigma_{Load} = 0.5V_p\sigma_M \quad (2)$$

The strengthening of thermal mismatch on YS can be calculated by formula (3)[64], and the results are 15.9 MPa and 12.6 MPa for the T6ACand T20AC composites, respectively:

$$\Delta\sigma_{CTE} = \sqrt{3}\beta G_M b\sqrt{\frac{12V_p\Delta T\Delta C}{(1-V_p)bd_{Ti}}} \quad (3)$$

Therefore, the theoretical YS increase of the $(Ti+Al)_p$/AZ31 can be expressed by formula (4):

$$\Delta\sigma = \Delta\sigma_{H-P} + \Delta\sigma_{Load} + \Delta\sigma_{CTE} \quad (4)$$

According to the calculation results, fine grain strengthening is the main strengthening mechanism. In the toughening mechanism of

Table 3
Parameters for calculating the above equation.

Parameter	Description	Value	Reference/Comment
K	Hall-Patch coefficient of AZ31	0.13 MPa•$m^{1/2}$	[21]
d_{AZ31}	Average grain size of AZ31	3.3 μm and 6.5 μm	calculated
d_{Ti}	Average particle size of Ti	32.9 μm	calculated
V_p	Volume fraction of particles	15 % and 10 %	calculated for T6AC, T20AC
β	Constant	1.25	[65]
b	Magnitude of Burgers Vector	3.2×10^{-10} m	[65]
G_M	The shear modulus of AZ31	18 GPa	[66]
ΔT	$T_{solidus\ temperature}$ - $T_{room\ temperature}$	472 K	calculated
ΔC	CTE of (AZ31 - Ti)	(26.5–9.4)μm/m•K	calculated

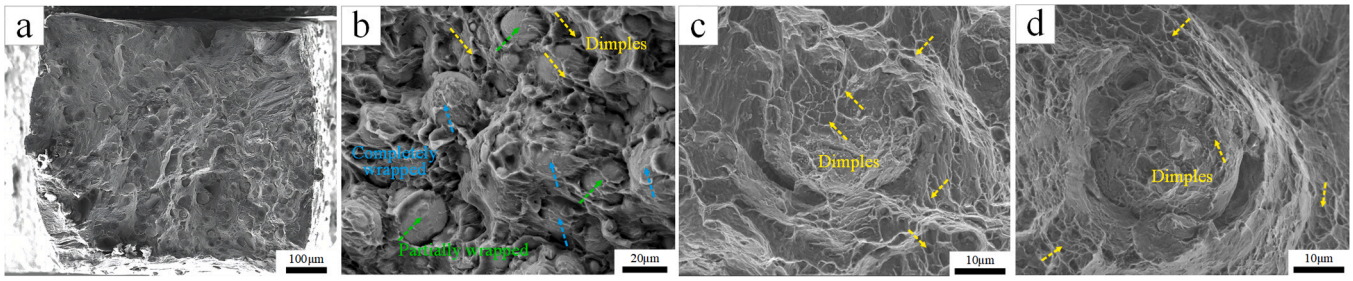


Fig. 16. Typical fracture characteristics of $(Ti+Al)_p$/AZ31 composites: (a) overview, (b) fracture morphology of completely and partially wrapped Ti particles, (c,d) dimples around completely wrapped Ti particles.

$(Ti+Al)_p$/AZ31 composite material, fine grain strengthening accounts for the main contribution, with the fine grain strengthening values of T6AC and T20AC accounting for 65.9 % and 60.0 % of the theoretical yield strength increase, respectively. Fine grain strengthening improves the plasticity and toughness of materials through a dual effect: on the one hand, high melting point Ti particles act as the core of heterogeneous nucleation during the initial solidification stage, promoting the nucleation of α-Mg phase; On the other hand, another issue is that Ti particles are located at the forefront of the solid-liquid interface during the solidification process, hindering grain growth. Therefore, refining the matrix grains is an essential step in the preparation process of composite materials.The theoretical$\Delta\sigma$values of T6AC and T20AC are 74.2 MPa and 47.2 MPa, respectively, while the experimental values of YS increase were 60.7 MPa and 38.5 MPa, respectively. There is a small deviation between the theoretical and experimental values because the theoretical model is considered that all the reinforcements are evenly dispersed in the molten pool. But actually there are imperfect local uniformity exists in multi-pass welds of the $(Ti+Al)_p$/AZ31 composites, which may reduce the effect of strengthening mechanism.

5. Conclusions

Al particles acted as the intermediate of Ti and Mg and improved the interface bonding and comprehensive performance of $(Ti+Al)_p$/AZ31. This research proposes a new solution for the further design and application of MMCs. The main conclusions are as follows:

(1) Under appropriate laser melt injection process conditions, large-area $(Ti+Al)_p$/AZ31 composites were well formed with no microscopic defects.

(2) Al particles of adjustable mass fraction acted as the intermediate of Ti and Mg and participated in the micro molten pool metallurgical reaction to form the transitional Al_3Ti layer with an average thickness of about 34 nm and a series of interfacial precipitates. These coherent Ti/Al_3Ti interface and semi-coherent $TiMnSi_2$/Mg_2Si and $TiMnSi_2$/Ti interfaces bridged the Ti particles and Mg to form a strong metallurgical interfacial bonding as well as participate in deformation coordination.

(3) $(Ti+6\ wt\%Al)_p$/AZ31 composites show excellent comprehensive tensile mechanical properties with YS, UTS, and EL reaching 186.6 MPa, 243.6 MPa, and 17.2 %, respectively, The YS and UTS are respectively 48.2 % and 21.8 % higher than those of the hot-rolled AZ31. The fine grain strengthening, load transfer strengthening, and thermal mismatch strengthening, each contributes 48.9 MPa, 9.4 MPa, and 15.9 MPa to the YS increasement, respectively, resulting in typical plastic fracture along 45° direction from the loading direction, and lots of dimples as well as Ti particles wrapped by the AZ31 matrix in the fracture.

(4) Compared with the hot-rolled AZ31, the $(Ti+Al)_p$/AZ31 composites have better wear resistance, a more stable wear process, a lower COF, as well as less and shallower furrows on the worn surface. The main reasons are that the unmelted Ti particles distributed within the molten pool are a harder phase, which hinders the frictional movement as well as the peeling off of the Ti particles.

CRediT authorship contribution statement

Zhenzhen Gui: Writing – review & editing, Writing – original draft, Supervision, Project administration, Methodology, Funding acquisition. **Dejian Liu:** Methodology, Investigation, Formal analysis. **Tao Zou:** Investigation, Formal analysis. **Dexin Chen:** Investigation, Data curation. **Fan Zhang:** Writing – review & editing, Supervision, Methodology. **Liu Cao:** Investigation, Formal analysis. **Chaowen Guo:** Writing – review & editing, Writing – original draft, Data curation. **Tao Zhang:** Project administration, Methodology, Funding acquisition, Conceptualization. **Jianhui Zhang:** Investigation, Data curation. **Teng Shen:** Investigation, Funding acquisition.

Declaration of Competing Interest

The authors declared that they have no conflicts of interest to this work. The manuscript is approved by all authors for publication. I would like to declare on behalf of my co-authors that the work described was original research that has not been published previously, and not under consideration for publication elsewhere, in whole or in part. All the authors listed have approved the manuscript that is enclosed.

Acknowledgements

This work was financially supported by the Guangdong Basic and Applied Basic Research (No. 2022A1515010265), the Science and Technology Planning Project of Guangdong Province (No. 2024A0505040017), the Science and Technology Program of Guangzhou City Joint with Universities (No. 2025A03J3107), the National Natural Science Foundation of China (No. 52371104, No. 52005116), and the Research and Integrated Application of Hardware Knife and Shear Materials, Forming Processing and Equipment Control Technology (No. RCZX2023003).

References

[1] H. Zhan, J. Zhang, J. Miao, C. Wang, G. Zeng, J. Wang, A. Luo, A low-cost Mg–Al–Mn–Zn alloy for automotive road wheel applications, Mater. Sci. Eng. A. 897 (2024) 146321, https://doi.org/10.1016/j.msea.2024.146321.
[2] S. Wang, H. Pan, D. Xie, D. Zhang, J. Li, H. Xie, Y. Ren, G. Qin, Grain refinement and strength enhancement in Mg wrought alloys: a review, J. Magnes. Alloy 11 (11) (2023) 4128–4145, https://doi.org/10.1016/j.jma.2023.11.002.
[3] M. Subramani, S.J. Huang, K. Borodianskiy, Effect of WS_2 nanotubes on the mechanical and wear behaviors of AZ31 stir casted magnesium metal matrix composites, J. Compos. Sci. 6 (7) (2022) 182, https://doi.org/10.3390/jcs6070182.
[4] S. Huang, M. Subramani, K. Borodianskiy, P. Immanuel, C. Chiang, Effect of equal channel angular pressing on the mechanical properties of homogenized hybrid AZ61 magnesium composites, Mater. Today Commun. 34 (2023) 104974, https://doi.org/10.1016/j.mtcomm.2022.104974.
[5] L. Fan, Y. Xiong, Y. Zeng, R. Ni, Y. Zhang, L. Ren, H. Diering, Y. Huang, G. Quan, X. Zhang, The strength-ductility synergy of magnesium matrix nanocomposite achieved by a dual-heterostructure, J. Mater. Sci. Technol. 215 (2025) 296–314, https://doi.org/10.1016/j.jmst.2024.07.027.
[6] L. Gu, B. Zhou, G. Zhu, J. Wang, J. Wang, L. Zhou, X. Zeng, Study of the micro-yielding behavior in a SiCp/Mg-Zn-Ca composite using synchrotron radiation diffraction, J. Mater. Sci. 9 (5) (2024) 1948–1957, https://doi.org/10.1007/s10853-023-09236-2.
[7] P. Emadi, B. Andilab, K. Borodianskiy, C. Ravindran, Strengthening of Mg-Al-Zn-Mn alloy using SiC/Al nanocomposite extrusion, J. Alloy. Compd. 922 (2022) 166243, https://doi.org/10.1016/j.jallcom.2022.166243.
[8] Z. Zhu, K. Nie, K. Deng, J. Han, Fabrication of biodegradable magnesium matrix composite with ultrafine grains and high strength by adding TiC nanoparticles to Mg-1.12 Ca-0.84 Zn-0.23 Mn (at%) alloy, Mater. Sci. Eng. C. 107 (2020) 110360, https://doi.org/10.1016/j.msec.2019.110360.
[9] E.G. Zemtsova, D.V. Yurchuk, P.E. Morozov, P.M. Korusenko, V.K. Kudymov, V. M. Smirnov, Features of the synthesis of the dispersed TiC phase with nickel nanostructures on the surface to create an aluminum-based metal composite, Nanomaterials 11 (10) (2021) 2499, https://doi.org/10.3390/nano11102499.
[10] M. Paidar, D. Bokov, S. Mehrez, O.O. Ojo, V.V. Ramalingam, S. Memon, Improvement of mechanical and wear behavior by the development of a new tool for the friction stir processing of Mg/B4C composite, Surf. Coat. Tech. 426 (2021) 127797, https://doi.org/10.1016/j.surfcoat.2021.127797.
[11] L. Gu, X. Shang, J. Wang, Z. Zhao, X. Zeng, W. Ding, The influence of SiC-Al2O3 reinforcements on the deformation and fracture mechanism of thixomolded Mg-based composite, J. Mater. Sci. 59 (22) (2024) 9892–9907, https://doi.org/10.1007/s10853-024-09386-x.
[12] H. Wu, Y. Zheng, J. Zhang, G. Zhang, Z. Ke, X. Xu, X. Lu, Influence of multi-step sintering on microstructural evolution and interfacial characteristics of Mo2FeB2-based cermets, J. Am. Ceram. Soc. 103 (10) (2020) 6040–6049, https://doi.org/10.1111/jace.17315.
[13] J. Li, B. Fu, T. Dong, G. Li, Y. Zhang, Y. Liu, J. Liu, Structural characterization and reaction mechanism of the Ti/SiC gradient material with Mg2Si additive fabricated by reaction sintering, J. Mater. Res. Technol. 25 (2023) 657–666, https://doi.org/10.1016/j.jmrt.2023.05.180.
[14] Y. Hong, X. Chen, G. Huang, J. Song, J. She, J. Tan, K. Zheng, Y. Jin, B. Jiang, F. Pan, Microstructures and mechanical properties of titanium-reinforced magnesium matrix composites: Review and perspective, J. Magnes. Alloy 10 (9) (2022) 2311–2333, https://doi.org/10.1016/j.jma.2022.07.008.
[15] Z. Gui, Y. Lu, H. Chen, L. Cao, Z. Kang, G. Wen, D. Liu, Preparation and properties of TiP/Mg-RE composites through laser melt injection, Mater. Sci. Eng. B. 287 (2023) 116095, https://doi.org/10.1016/j.mseb.2022.116095.

[16] Y. Wang, J. Li, B. Guan, B. Tang, H. Luo, Y. Lu, H. Yu, W. He, X. Chen, K. Zheng, Microstructure and mechanical properties of hybrid graphene nanoplatelets/titanium particles reinforced AZ91 laminated composite, Mater. Sci. Eng. A. 856 (2022) 144017, https://doi.org/10.1016/j.msea.2022.144017.
[17] Y. Fan, K. Deng, C. Wang, K. Nie, Q. Shi, Work hardening and softening behavior of Mg-Zn-Ca alloy influenced by deformable Ti particles, Mater. Sci. Eng. A. 833 (2022) 142336, https://doi.org/10.1016/j.msea.2021.142336.
[18] M. Maleki, F. Jamei, M. Emamy, H. Mirzadeh, Microstructure and mechanical properties of as-cast and wrought Mg-Ni in-situ formed alloys, Mater. Sci. Tech. -Lond. 39 (8) (2023) 985–993, https://doi.org/10.1080/02670836.2022.2154934.
[19] M.A. bin Ariffin, M.R. bin Muhamad, S. Raja, M.F. Jamaludin, F. Yusof, T. Suga, H. Liu, Y. Morisada, H. Fujii, Friction stir alloying of AZ61 and mild steel with Cu-CNT additive, J. Mater. Res. Technol. 21 (2022) 2400–2415, https://doi.org/10.1016/j.jmrt.2022.10.082.
[20] Q. Wang, P. Han, W. Niu, N. Li, X. Mao, High-speed impact behavior of cold-sprayed Fe-based amorphous particle on Mg alloy substrate, Intermetallics 163 (2023) 108070, https://doi.org/10.1016/j.intermet.2023.108070.
[21] D. Pu, S. Wu, H. Yang, X. Chen, J. Li, X. Feng, K. Zheng, F. Pan, Effect of Ti particles on microstructure and mechanical properties of TiP/AZ91 composites, J. Mater. Res. Technol. 22 (2023) 1362–1374, https://doi.org/10.1016/j.jmrt.2022.12.028.
[22] B. Tang, J. Li, J. Ye, H. Luo, Y. Wang, B. Guan, Y. Lu, X. Chen, K. Zheng, F. Pan, Strengthening mechanism and microstructure of deformable Ti particles reinforced AZ91 composite, Acta Metall. Sin. -Engl. 35 (12) (2022) 1935–1945, https://doi.org/10.1007/s40195-022-01428-0.
[23] H. Yu, Y. Sun, L. Hu, Z. Wan, H. Zhou, Microstructure and properties of mechanically milled AZ61 powders dispersed with submicron/nanometer Ti particulates, Mater. Charact. 127 (2017) 272–278, https://doi.org/10.1016/j.matchar.2017.03.017.
[24] J. Ye, J. Li, H. Luo, J. Tan, X. Chen, B. Feng, K. Zheng, F. Pan, Effect of micron-Ti particles on microstructure and mechanical properties of Mg-3Al-1Zn based composites, Mater. Sci. Eng. A. 833 (2022) 142526, https://doi.org/10.1016/j.msea.2021.142526.
[25] J. Ye, X. Chen, H. Luo, J. Zhao, J. Li, J. Tan, H. Yang, B. Feng, K. Zheng, F. Pan, Microstructure, mechanical properties and wear resistance of Ti particles reinforced AZ31 magnesium matrix composites, J. Magnes. Alloy 10 (8) (2022) 2266–2279, https://doi.org/10.1016/j.jma.2022.06.012.
[26] Jun Li, Y. Huang, F. Wang, F. Wang, X. Meng, L. Wan, Z. Dong, Enhanced strength and ductility of friction-stir-processed Mg-6Zn alloys via Y and Zr co-alloying, Mater. Sci. Eng. A. 773 (2020) 138877, https://doi.org/10.1016/j.msea.2019.138877.
[27] C. Zang, J. Liu, C. Tan, K. Zhang, X. Song, B. Chen, L. Li, J. Feng, Laser conduction welding characteristics of dissimilar metals Mg/Ti with Al interlayer, J. Manuf. Process. 32 (2018) 595–605, https://doi.org/10.1016/j.jmapro.2018.03.019.
[28] P. Wang, Z. Chen, H. Huang, J. Lin, B. Li, Q. Liu, Fabrication of Ti/Al/Mg laminated composites by hot roll bonding and their microstructures and mechanical properties, Chin. J. Aeronaut. 34 (8) (2021) 192–201, https://doi.org/10.1016/j.cja.2020.08.044.
[29] P. Wang, H. Huang, J. Liu, Q. Liu, Z. Chen, Microstructure and mechanical properties of Ti6Al4V/AA6061/AZ31 laminated metal composites (LMCs) fabricated by hot roll bonding, J. Alloy. Compd. 861 (2021) 157943, https://doi.org/10.1016/j.jallcom.2020.157943.
[30] E. Hajjari, M. Divandari, S. Razavi, S. Emami, T. Homma, S. Kamado, Dissimilar joining of Al/Mg light metals by compound casting process, J. Mater. Sci. 46 (2011) 6491–6499, https://doi.org/10.1007/s10853-011-5595-4.
[31] S. Zhang, P. Yuan, X. Wang, T. Wang, L. Zhao, C. Cui, Fabrication and Properties of Zn-3Mg-1Ti Alloy as a Potential Biodegradable Implant Material, Materials 15 (3) (2022) 940, https://doi.org/10.3390/ma15030940.
[32] N. Kumar, A. Bharti, Y. Chandra, Binding effect of copper on physical, mechanical, and thermal properties of Mg/Ti/Cu composites, Powder Met. Met. C. 62 (9) (2024) 597–610, https://doi.org/10.1007/s11106-024-00420-w.
[33] Y. Lian, Z. Gan, C. Yu, D. Kats, W.K. Liu, G.J. Wagner, A cellular automaton finite volume method for microstructure evolution during additive manufacturing, Mater. Des. 169 (2019) 107672, https://doi.org/10.3390/ma15030940.
[34] J. Wang, R. Zhu, Y. Liu, L. Zhang, Understanding melt pool characteristics in laser powder bed fusion: an overview of single-and multi-track melt pools for process optimization, APM 2 (4) (2023) 100137, https://doi.org/10.1016/j.matdes.2019.107672.
[35] S. Liu, H. Guo, Balling Behavior of Selective Laser Melting (SLM) Magnesium Alloy, Materials 13 (16) (2020) 3632, https://doi.org/10.3390/ma13163632.
[36] I.F. Bainbridge, J.A. Taylor, The surface tension of pure aluminum and aluminum alloys, Metall. Mater. Trans. 44 (2013) 3901–3909, https://doi.org/10.3390/ma13163632.
[37] G. Huang, D. Gu, D. Dai, L. Yuan, R. Wang, K. Xiong, Microstructure evolution and underlying thermal behavior of high-content TiC reinforced titanium matrix composites fabricated by laser directed energy deposition, J. Mater. Res. Technol. 23 (2023) 3007–3022, https://doi.org/10.1007/s11661-013-1696-9.
[38] Y. Mishin, C. Herzig, Diffusion in the Ti-Al system, Acta Mater. 48 (3) (2000) 589–623, https://doi.org/10.1016/j.jmrt.2023.01.226.
[39] W. Chen, H. Hou, Y. Zhang, W. Liu, Y. Zhao, Thermal and solute diffusion in α-Mg dendrite growth of Mg-5wt% Zn alloy: a phase-field study, J. Mater. Res. Technol. 24 (2023) 8401–8413, https://doi.org/10.1016/S1359-6454(99)00400-0.
[40] H. Xue, C. Yang, F. De Geuser, P. Zhang, J. Zhang, B. Chen, F. Liu, Y. Peng, J. Bian, G. Liu, Highly stable coherent nanoprecipitates via diffusion-dominated solute uptake and interstitial ordering, Nat. Mater. 22 (4) (2023) 434–441, https://doi.org/10.1016/j.jmrt.2023.05.024.
[41] C. Zhang, J.D. Robson, S.J. Haigh, P.B. Prangnell, Interfacial segregation of alloying elements during dissimilar ultrasonic welding of AA6111 aluminum and Ti6Al4V titanium, Metall. Mater. Trans. 50 (2019) 5143–5152, https://doi.org/10.1038/s41563-022-01420-0.
[42] A. Meher, M.M. Mahapatra, P. Samal, P.R. Vundavilli, Study on effect of TiB2 reinforcement on the microstructural and mechanical properties of magnesium RZ5 alloy based metal matrix composites, J. Magnes. Alloy 8 (3) (2020) 780–792, https://doi.org/10.1016/j.jma.2020.04.003.
[43] S. Seetharaman, J. Subramanian, M. Gupta, A.S. Hamouda, Influence of micron-Ti and nano-Cu additions on the microstructure and mechanical properties of pure magnesium, Metals 2 (3) (2012) 274–291, https://doi.org/10.3390/met2030274.
[44] X. Ai, G. Quan, Effect of Ti on the mechanical properties and corrosion of cast AZ91 magnesium alloy, Open Mater. Sci. J. 6 (1) (2012), https://doi.org/10.2174/1874088X01206010006.
[45] S. Sankaranarayanan, S. Jayalakshmi, M. Gupta, Effect of addition of mutually soluble and insoluble metallic elements on the microstructure, tensile and compressive properties of pure magnesium, Mater. Sci. Eng. A. 530 (2011) 149–160, https://doi.org/10.1016/j.msea.2011.09.066.
[46] W. Guo, Q. Wang, B. Ye, H. Zhou, Enhanced microstructure homogeneity and mechanical properties of AZ31-Si composite by cyclic closed-die forging, J. Alloy. Compd. 552 (2013) 409–417, https://doi.org/10.1016/j.jallcom.2012.11.067.
[47] X. Wang, X. Wang, X. Hu, K. Wu, Effects of hot extrusion on microstructure and mechanical properties of Mg matrix composite reinforced with deformable TC4 particles, J. Magnes. Alloy 8 (2) (2020) 421–430, https://doi.org/10.1016/j.jma.2019.05.015.
[48] W. Qiu, Z. Liu, R. Yu, J. Chen, Y. Ren, J. He, W. Li, C. Li, Utilization of VN particles for grain refinement and mechanical properties of AZ31 magnesium alloy, J. Alloy. Compd. 781 (2019) 1150–1158, https://doi.org/10.1016/j.jallcom.2018.12.124.
[49] P. Gao, S. Han, Y. Zhang, B. Fang, X. Zhang, X. Wang, H. Ding, K. Zheng, F. Pan, Investigation on the interface bonding and reinforcement mechanism of nano Ti/AZ31 magnesium matrix composites, J. Mater. Res. Technol. 30 (2024) 4908–4919, https://doi.org/10.1016/j.jmrt.2024.04.201.
[50] H. Hao, X. Liu, C. Fang, X. Zhang, Effect of in-situ Al2Y particles on the as-cast/as-rolled microstructure and mechanical properties of AZ31 alloy, Mater. Sci. Eng. A. 698 (2017) 27–35, https://doi.org/10.1016/j.msea.2017.04.114.
[51] X. Liu, Z. Zhang, Q. Le, L. Bao, The effects of ZnO particles on the grain refinement and mechanical properties of AZ31 magnesium alloys, T. Indian. I. Met. 69 (2016) 1911–1918, https://doi.org/10.1007/s12666-016-0850-7.
[52] C. Lin, W. Wu, Y. Han, J. Liu, M. Zhang, Q. Wang, X. Li, Orderly nucleation and competitive growth behaviors of Ti-Al intermetallic compounds in Ti/TiAl3 diffusion couple under high temperature, J. Alloy. Compd. 939 (2023) 168815, https://doi.org/10.1016/j.jallcom.2023.168815.
[53] U. Kattner, J. Lin, Y. Chang, Thermodynamic assessment and calculation of the Ti-Al system, Metall. Trans. A. 23 (1992) 2081–2090, https://doi.org/10.1007/BF02646001.
[54] H. Wang, Y. Zhang, S. Yang, B. Liu, Effects of slurry pack cementation temperature on microstructure and wear resistance of Ti-Al co-deposited coating on copper plated nickel layer, Trans. Nonferrous Met. Soc. China 24 (2) (2014) 449–454, https://doi.org/10.1016/S1003-6326(14)63081-8.
[55] Y. Cao, P. Wang, Y. Xu, T. Li, J. Liu, J. Duan, D. Zhang, S. Zhou, First-principles calculations to investigate adhesion strength, stability and electronic properties of Al (111)/TiAl3 (112) interface, Indian. J. Phys. 97 (6) (2023) 1679–1685, https://doi.org/10.1007/s12648-022-02538-2.
[56] C. Lu, J. Yang, Y. Zhao, X. Lei, J. Huang, S. Chen, Z. Ye, Influence of applied electric field on atom diffusion behavior and mechanism for W/NiFe interface in diffusion bonding of Steel/NiFe interlayer/W by spark plasma sintering, Appl. Surf. Sci. 541 (2021) 148516, https://doi.org/10.1016/j.apsusc.2020.148516.
[57] M. Liu, C. Zhang, Z. Meng, G. Zhao, L. Chen, TiAl3 nucleation mechanism and atomic-scale interface features in the Al/Ti composite structures, Compos. Part. B-Eng. 226 (2021) 109331, https://doi.org/10.1016/j.compositesb.2021.109331.
[58] H. Luo, J. Li, J. Ye, Y. Lu, J. Tan, J. Song, X. Chen, K. Zheng, F. Pan, Influence of Ti-6Al-4V particles on the interfacial microstructure and strength-ductility synergetic mechanism of AZ91 magnesium alloy, Mater. Charact. 191 (2022) 112154, https://doi.org/10.1016/j.matchar.2022.112154.
[59] Y. Song, Z. Dou, T. Zhang, Y. Liu, G. Wang, First-principles calculation on the structural, elastic and thermodynamic properties of Ti-Al intermetallics, Mater. Res. Express 6 (10) (2019) 1065a4, https://doi.org/10.1088/2053-1591/ab3e11.
[60] T. Murakumo, T. Kobayashi, Y. Koizumi, H. Harada, Creep behaviour of Ni-base single-crystal superalloys with various γ′ volume fraction, Acta Mater. 52 (12) (2004) 3737–3744, https://doi.org/10.1016/j.actamat.2004.04.028.
[61] A.C. Yeh, A. Sato, T. Kobayashi, H. Harada, On the creep and phase stability of advanced Ni-base singlecrystal superalloys, Mater. Sci. Eng. A. 490 (1-2) (2008) 445–451, https://doi.org/10.1016/j.msea.2008.02.008.
[62] J. Yi, H. Liao, C. Chang, X. Yan, L. Min, K. Zhou, Reinforcing effects of nano-WC in AlSi10Mg alloy assisted by in-situ surface modification approach, Trans. Nonferrous Met. Soc. China 34 (1) (2024) 50–64, https://doi.org/10.1016/S1003-6326(23)66381-2.
[63] H. Wang, W. Su, J. Liu, G. Li, Y. Liu, P. Zhou, Microstructure and properties of FeCoNiCrMn and Al2O3 hybrid particle-reinforced aluminum matrix composites fabricated by microwave sintering, J. Mater. Res. Technol. 24 (2023) 8618–8634, https://doi.org/10.1016/j.jmrt.2023.05.100.
[64] J. Cui, H. Yang, Y. Zhou, J. Tan, X. Chen, J. Song, G. Huang, K. Zheng, Y. Jin, B. Jiang, Optimizing the microstructures and enhancing the mechanical properties

of AZ81 alloy by adding TC4 particles, Mater. Sci. Eng. A. 863 (2023) 144518, https://doi.org/10.1016/j.msea.2022.144518.
[65] A. Khandelwal, K. Mani, N. Srivastava, R. Gupta, G. Chaudhari, Mechanical behavior of AZ31/Al2O3 magnesium alloy nanocomposites prepared using ultrasound assisted stir casting, Compos Part B-Eng. 123 (2017) 64–73, https://doi.org/10.1016/j.compositesb.2017.05.007.
[66] W. Wen, F. Yuan, P. Pai, Z. Zhang, H. Peng, T. Zhang, Z. Liu, X. Guan, W. Zhi, Q. Ke, Microstructure, mechanical and wear properties of AZ31/CoCrFeNi composites fabricated by friction stir processing, Trans. Nonferrous Met. Soc. China 33 (8) (2023) 2328–2339, https://doi.org/10.1016/S1003-6326(23)66262-4.